Article

Adaptive Turbulence Model for Leading Edge Vortex Flows Preconditioned by a Hybrid Neural Network

Moritz Zieher *,† and Christian Breitsamter †

Chair of Aerodynamics and Fluid Mechanics, Technical University of Munich, 85748 Garching bei München, Germany; christian.breitsamter@tum.de

* Correspondence: moritz.zieher@tum.de; Tel.: +49-(89)-289-16153

† These authors contributed equally to this work.

Abstract: Eddy-viscosity-based turbulence models provide the most commonly used modeling approach for computational fluid dynamics simulations in the aerospace industry. These models are very accurate at a relatively low cost for many cases but lack accuracy in the case of highly rotational leading edge vortex flows for mid to low aspect-ratio wings. An enhanced adaptive turbulence model based on the one-equation Spalart–Allmaras turbulence model is fundamental to this work. This model employs several additional coefficients and source terms, specifically targeting vortex-dominated flow regions, where these coefficients can be calibrated by an optimization procedure based on experimental or high-fidelity numerical data. To extend the usability of the model from single or cluster-wise calibrated cases, this work presents a preconditioning approach of the turbulence model via a neural network. The neural network provides a case-unspecific calibration approach, enabling the use of the model for many known or unknown cases. This extension enables aircraft design teams to perform low-cost Reynolds-averaged Navier–Stokes simulations with increased accuracy instead of complex and costly high-fidelity simulations.

Keywords: turbulence modeling; vortex flows; multiple swept delta wings; machine learning; neural networks

1. Introduction

Reynolds Averaged Navier–Stokes Equation (RANS) equations, in combination with eddy viscosity turbulence models based on the Boussinesq assumption, build the foundation of computational fluid dynamics simulations in aircraft development. On the one hand, these simulations can predict aerodynamic behavior at satisfactory accuracy levels for most investigated configurations while providing comparatively low costs and robustness. On the other hand, the models lack accuracy at higher angles of attack for leading-edge vortex flow systems of mid to low aspect-ratio delta wing configurations since they cannot represent the effects on streamline curvature and system rotation. Shur et al., introduced a streamline curvature correction (SARC) approach by multiplying the production term in the original Spalart–Allmaras (SA) turbulence model by a rotation function [1]. Further, this modification has been implemented to the Shear Stress Transport (SST) turbulence model of Menter [2,3]. Two approaches to account for the effects of rotation and curvature are explored by Arolla et al. [4]. The "Modified coefficients approach" aims to alter the growth rate of the turbulent kinetic energy, whereas the "Bifurcation approach" adjusts the eddy viscosity coefficient such that the equilibrium solution bifurcates from healthy to decaying solutions. While most of the available turbulence model corrections for this type of flow aim at maintaining the globality of the fundamental turbulence model, Moioli et al., developed an adaptive turbulence model based on the one-equation SA turbulence model [5,6]. Moioli et al., introduced additional source terms controlled by model coefficients and a switch

factor (i–vii in Equation (1)), which is only effective in vortex-dominated flow regions and switches off the added source terms in unaffected regions of the flow.

$$
\frac{D\tilde{v}}{Dt} = c_{b1}\tilde{S}(1 - f_{t2})\tilde{v}
$$

$$
- \left[\overbrace{c_{bv1}\tilde{\xi}S\tilde{v}}^{i} + \overbrace{c_{bv2}\tilde{\xi}^{\frac{1}{2}}S\tilde{v}}^{ii} + \overbrace{c_{bv3}\tilde{\xi}^{2}S\tilde{v}}^{iii} + \overbrace{c_{bv4}\left(min\left(\frac{1}{\tilde{\xi}}, c_{vr,lim}\right)\right)\tilde{\xi}_{sw}S\tilde{v}}^{iv} + \overbrace{c_{bvh1}\tilde{\xi}\tilde{H}\tilde{v}}^{v} \right.
$$

$$
\left. + \overbrace{c_{bvh2}\left[max\left(min\left(\frac{1}{\tilde{H}}, 1.0\right), 0.0\right)\right]\tilde{\xi}\omega\tilde{v}}^{vi} + \overbrace{c_{bvb}|\tilde{\xi}\nabla V\omega_{dir}|\tilde{v}}^{vii} \right]
$$

$$
+ \frac{1}{\sigma}\left[\nabla \cdot ((\nu + \tilde{v})\nabla\tilde{v}) + c_{b2}(\tilde{v})^2\right] - \left(c_{w1}f_w - \frac{c_{b1}}{\kappa^2}f_{t2}\right)\left[\frac{\tilde{v}}{d}\right]^2
$$

(1)

The model coefficients can be set via a gradient descent approach optimization procedure based on experimental or high-fidelity simulation data. Further, in the field of turbulence modeling, Duraisamy et al., pointed out the expanding importance of data-driven models and techniques in computational fluid dynamics (CFD) [7]. The increase in computational power, e.g., on the side of graphical processing units, leads to the development of new machine learning algorithms and enables the usage of existing ones, taking advantage of the vast amount of available data from experimental and numerical studies. Deep learning architectures have been shown to represent high-level abstractions in various fields [8]. Sabater et al., develop three fast prediction tools to predict aircraft surface pressure distribution using different machine learning techniques [9]. Their study shows that deep-learning methods outperform others by accurately predicting shock wave locations and strength in transonic flows. The characteristics of transonic buffet are predicted by a reduced-order modeling (ROM) framework based on a long short-term memory (LSTM) neural network in the work of Zahn et al. [10]. Zhang et al., used convolutional neural network (CNN) architectures to predict lift coefficient based on airfoil shape and flow conditions.

The objective of this work is to develop a data-driven methodology for the preconditioning of the enhanced SA turbulence model (Equation (1)) by Moioli et al., and highlight the benefits of a low-cost preconditioning framework [5]. While the enhanced model is specially tailored for leading-edge vortex flows of mid to low aspect-ratio delta wings, the framework shall be independent of the aircraft configuration. The predictive capabilities are discussed for a generic triple delta wing test case in Section 7.

2. Test Cases: Generic Multiple Swept Delta Wings

This study considers generic wing-fuselage configurations in the form of triple and double delta wing configurations with varying leading-edge sweep angles. The wind tunnel models consist of a fuselage and interchangeable flat plate wings with sharp leading-edges. Each configuration type is also equipped with deflectable control surfaces, e.g., levcons for triple delta wings and slats for double and triple delta wings.

These geometries were and are subject to a common research program in cooperation with Airbus Defence and Space and the German Aerospace Center and are further embedded in the NATO AVT-316 task group [11]. Various experimental and numerical studies have been performed for a range of configurations [12–15]. Table 1 lists the most important geometrical parameters of the two configuration types. An overview of the two different types is also depicted in Figure 1a,b. For this study, five triple and five double delta wing plan forms serve as training datasets for the machine learning framework. Further, the designation of different configurations follows the initial convention developed by Airbus Defence and Space. E.g., the platform F3 607060 STLong LV00 SL00 FL00 describes a triple delta wing (F3) with a 60° levcon sweep angle φ_1, a 70° strake sweep angle φ_2, and a

main wing sweep angle of $\varphi_3 = 60°$. STLong designates the long strake section of the two possible values for l_2 in Table 1, whereas STShort would designate the shorter version. The abbreviations LV, SL, and FL, followed by the number 00, describe the zero deflection angles for the different available control surfaces levcon (LV), slat (SL), and flap (FL).

Table 1. Geometrical properties for the generic double and triple delta wing configurations (Figure 1).

	Double Delta	Triple Delta
c_r [m]	0.58–0.8	0.65–0.83
s [m]	0.29–0.468	0.32–0.53
S_{ref} [m^2]	0.25–0.35	0.29–0.43
Λ [$-$]	1.34–2.62	1.4–2.74
l_{tot} [m]	1.16	1.16
l_μ [m]	0.395–0.54	0.44–0.565
l_1/c_r [$-$]	0.125	-
l_2/c_r [$-$]	0.375/0.475	0.25/0.35
l_3/c_r [$-$]	0.35	0.35
φ_1 [°]	-	45–60
φ_2 [°]	70–75	70–75
φ_3 [°]	45–60	45–60

(**a**)   (**b**)
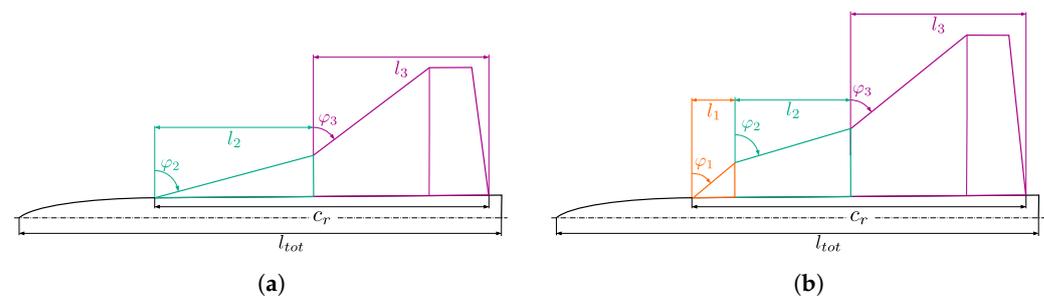
Figure 1. Generic multiple swept delta wing planforms with corresponding geometrical properties listed in Table 1. (**a**) Generic double delta wing. (**b**) Generic triple delta wing.

3. Numerical Setup

The TAU-Code (triangular adaptive upwind) developed by DLR is used as the fundamental flow solver. The DLR TAU-Code is widely accepted in the aviation industry and provides a tool to run complex flow simulations on structured and unstructured hybrid grids. It represents not one simple code but a modern software system to compute inviscid and viscous flows at various flow velocities for simple and complex geometries. The TAU system is composed of different modules and libraries to allow for the easier development, maintenance, and reuse of the code or parts of it. Single modules can be used as stand-alone tools with a specific file I/O or in combination with a Python scripting framework, allowing inter-module communication and enabling interaction with a started simulation [16]. The flow calculations are based on the dual grid approach, which gives good results for three-dimensional hybrid grids. The Runge–Kutta dual time stepping method or a backward Euler implicit scheme are used as a time-marching method to solve three-dimensional Navier–Stokes equations with LU-SGS (lower-upper symmetric Gauss-Seidel) or SGS iterations. The optimization process described in Section 5 is coupled with TAU via a Python framework (Python 3.8.16).

All simulations have been performed at a Mach number $M_\infty = 0.15$ and a Reynolds number $Re = 3 \cdot 10^6$ to resemble the experiments conducted in the wind tunnel of the Chair of Aerodynamics and Fluid Mechanics at the Technical University of Munich by Pfnür et al. [12]. The CENTAUR meshing software has been used to create numerical grids as hybrid unstructured grids with prism layers and tetraeders. A grid study has been performed for the generic double delta wing with a strake sweep angle of $\varphi_2 = 75°$ and a main wing sweep angle of $\varphi_3 = 52.5°$. Figure 2 presents the results of the conducted

gridstudy. For each of the five different grid resolutions, a simulation at the angle of attack $\alpha = [8°; 16°; 24°; 32°]$ has been performed. The lift coefficient results in the left part of Figure 2 show that all grid resolutions represent the experimentally obtained lift coefficient rather well. The results of the pitching moment coefficient in the right hand of Figure 2 show that all grid resolutions deviate from the experimental value. The results show that there is no improvement in accuracy from the fine grid level to the very fine grid level.

Considering the results of the grid study and the high number of simulations needed to generate the training dataset, the medium grid resolution has been selected. This grid level has $\approx 22 \cdot 10^6$ elements, and the numerical grids of all different configurations have been kept as similar as possible. Figure 3 shows a sample of the medium-sized double delta wing grid.
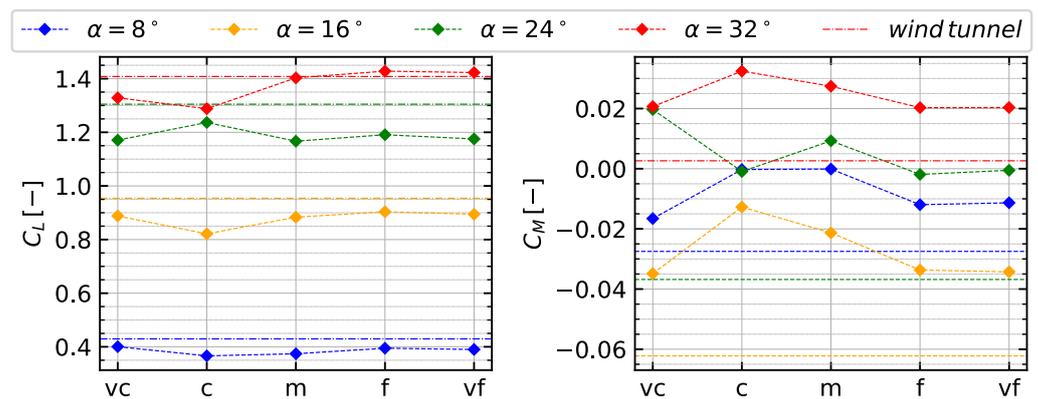
Figure 2. Gridstudy of an generic double delta wing. Lift coefficient C_L and pitching moment coefficient C_M for five grid resolution at angles of attack $\alpha = [8°; 16°; 24°; 32°]$. Grid levels: vc—very coarse; c—coarse; m—medium; f—fine; and vf—very fine.
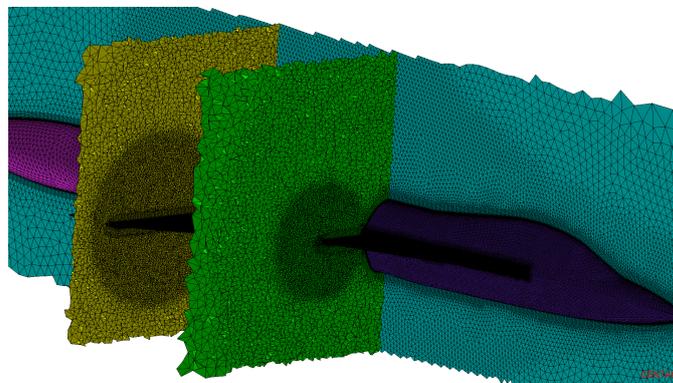
Figure 3. Three-dimensional isometric view of the medium-sized mesh of a double delta wing.

4. Adaptive Turbulence Model

The additional source terms of the adaptive turbulence model in Equation (1) are controlled via corresponding additional turbulence model coefficients and other flow quantities, limiting the added terms' influence region to vortex-dominated flow regions only. Thus, the vortex identifier ξ is the most important control quantity. Based on the works of Truesdell and Jeong et al., Moioli et al., implemented the vortex identifier quantity based on the definition that a vortex can be defined as the region where the kinematic vorticity number N_k is greater than one [17,18]. From the definition $N_k = \omega / S$, the vortex identifier is defined as,

$$\xi = max\left[\left(\left(\frac{\omega}{S + \epsilon}\right) - c_{vl}\right), 0.0\right]; \quad c_{vl} = 1, \tag{2}$$

where ϵ is a small number to avoid numerical overflow in the case the strain rate takes on values close to zero [5]. The offset by the c_{v1} coefficient is needed to remove the influence of terms multiplied by ξ in the boundary layer.

This work will focus on the terms *i*, *v*, and *vi* in Equation (1), which will be introduced in detail in the following. c_{bv1} is the first added source term, which is only influenced by the vortex identifier and is the most similar one to the original SA source term $c_{b1}\tilde{S}\tilde{v}$. Secondly, the coefficient c_{bvh1} is multiplied by ξ and the normalized helicity $\tilde{H}$. The Helicity $H = V \cdot \omega$ expresses the alignment of velocity and vorticity vectors. The unburst part of a vortex shows high axial and rotational velocities, where the vorticity is increased along axial direction [19]. Thus, the source term $c_{bvh1}\xi\tilde{H}\tilde{v}$ acts in regions of fully developed healthy vortices. To prevent the turbulence model from acting differently for right and left-rotating vortices, it is important to use the absolute value of the helicity since the quantity also considers the vortex's chirality. In order to non-dimensionalize all added quantities, the absolute value of helicity is normalized by the free-stream velocity, resulting in a final non-dimensional helicity $\tilde{H} = (V \cdot \omega)/U_\infty$. The flow regions downstream of vortex breakdown are influenced by an inverted helicity-based term and the coefficient c_{bvh2}. Caused by abrupt changes in rotational and axial velocities, vortex breakdown can be enclosed by regions of high-velocity gradients. Thus, the coefficient c_{bvb}, combined with the velocity gradient tensor and the vorticity direction, mainly influences regions near vortex breakdown. Figure 4 shows the influence of three additional turbulence model coefficients for an exemplary double delta wing configuration.
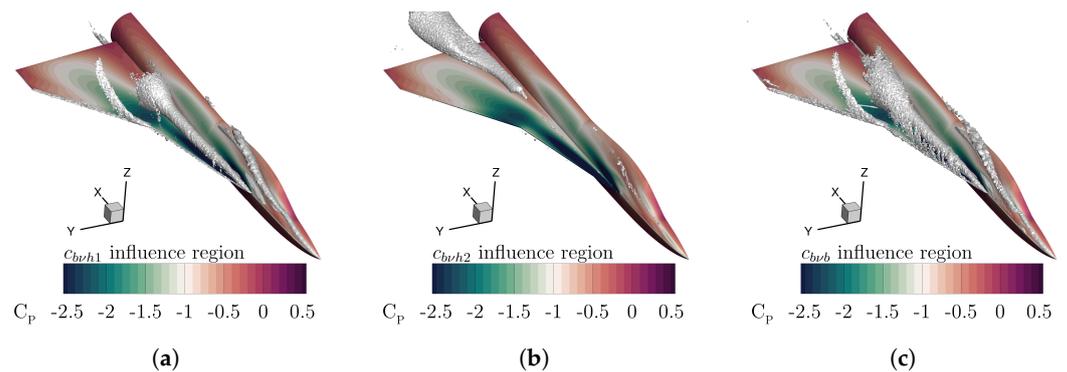
Figure 4. Influence regions of the additional turbulence model coefficients. (**a**) c_{bvh1} acts on fully developed vortices upstream of vortex breakdown. (**b**) c_{bvh2} influences mainly regions downstream of the vortex breakdown. (**c**) c_{bvb} acts in proximity the vortex breakdown.

5. Optimization of Additional Turbulence Model Coefficients

The coefficients of the additional source terms can be determined by an optimization scheme based on gradient descent optimization [5]. The iterative algorithm minimizes the objective function $\mathcal{E}(x)$, which is defined as the L-1 norm between numerical and experimental data and is defined as:

$$\mathcal{E}(x) = \frac{\sum_{i=1}^{k} \sum_{j=1}^{l} \left[\varepsilon_{exp}^{(i,j)} w_{dp}^{(i)} \right]}{mn \left(\sum_{i=1}^{m} w_{dp}^{(i)} \right)} \tag{3}$$

where k is the number of design points, e.g., angles of attack, and l is the number of experimental coefficients, e.g., the lift coefficient C_L and pitching moment coefficient C_M. The importance of experimental reference values can be adjusted by weighting factors $w_{dp}^{(i)}$. $\varepsilon_{exp}^{(i,j)}$ itself is the deviation of numerical from experimental coefficients.

Figure 5 depicts the optimization process flowchart, where a case is started by selecting a set of starting values $\vec{x}_0$.

```
┌─────────────┐
│    Start    │
└─────────────┘
```

Numerical simulations with selected starting values
of the coefficients $\vec{x}^{(0)} = \vec{x}_0$
Definition of increments $\Delta\vec{x}$ and relaxation factor α

Restart of all simulations with
$\vec{x}^{(i)}$ (base) and
$\vec{x}^{(i)} + \Delta\vec{x}$ (incremental)

Errors between numerical and experimental data
$\varepsilon^{(i)}(\vec{x})$ and $\varepsilon^{(i)}(\vec{x} + \Delta\vec{x})$

Estimation of the gradients and descent directions
$$\Delta\varepsilon^{(i)}(\vec{x}) = \frac{\varepsilon^{(i)}(x_j + \Delta x_j) - \varepsilon^{(i)}(x_j)}{\Delta x_j}$$

Computation of new set of coefficients
$$\vec{x}^{(i+1)} = \vec{x}^{(i)} + \alpha\Delta\varepsilon^{(i)}(\vec{x})$$

converged? no

yes

Optimised set of turbulence model coefficients $\vec{x}$

```
┌─────────────┐
│     End     │
└─────────────┘
```

Figure 5. Flowchart of the coefficient optimization procedure.

Further, different increments $\Delta\vec{x}$ for each coefficient and an overall relaxation factor α need to be defined. Based on the initial settings, a series of numerical simulations is started, where a base simulation with the currently defined turbulence model coefficients is executed first. After this first base simulation is finished, the so-called incremental simulations are started, where for each included turbulence model coefficient a simulation is started after the predefined increment alters the base coefficient. A second base simulation continues the first base simulation to keep a consistent base solution throughout the process. Once the second base and all incremental simulations have finished, the errors concerning the linked experimental reference values can be computed. Experimental values can consist of aerodynamic coefficients, integral forces, surface pressure distributions from time-resolved pressure sensitive paint (iPSP) or pressure tabs. Due to the availability of aerodynamic

coefficients for several configurations included in the generic wing-body platform described in Section 2, this type of reference value has been chosen.

From the computed errors, the gradients and descent directions can be computed. Finally, a new updated set of turbulence model coefficients is defined by:

$$\vec{x}^{(i+1)} = \vec{x}^{(i)} + \alpha \Delta \varepsilon^{(i)}(\vec{x}) \tag{4}$$

where α is the defined relaxation factor to avoid overshooting during the optimization procedure, which is set at $\alpha = 0.5$ for this study. Once the new set of coefficients has been defined, it needs to be checked if the results have converged. If a satisfying level of convergence is reached, the optimization is ended with the set of turbulence model coefficients. If no convergence is reached, the optimization loop is restarted with the new set of coefficients serving as the new base. Since the gradient descent approach is inherently local and converges to local minima, cases with different starting points x_0 should be run to increase the likelihood of finding a global optimum [5]. Figure 6 depicts a sample of an optimization run. The objective function $\mathcal{E}(x)$ is plotted versus the optimization iterations in the top part of the figure. The three additional turbulence values used are plotted against the corresponding iterations in the lower part.
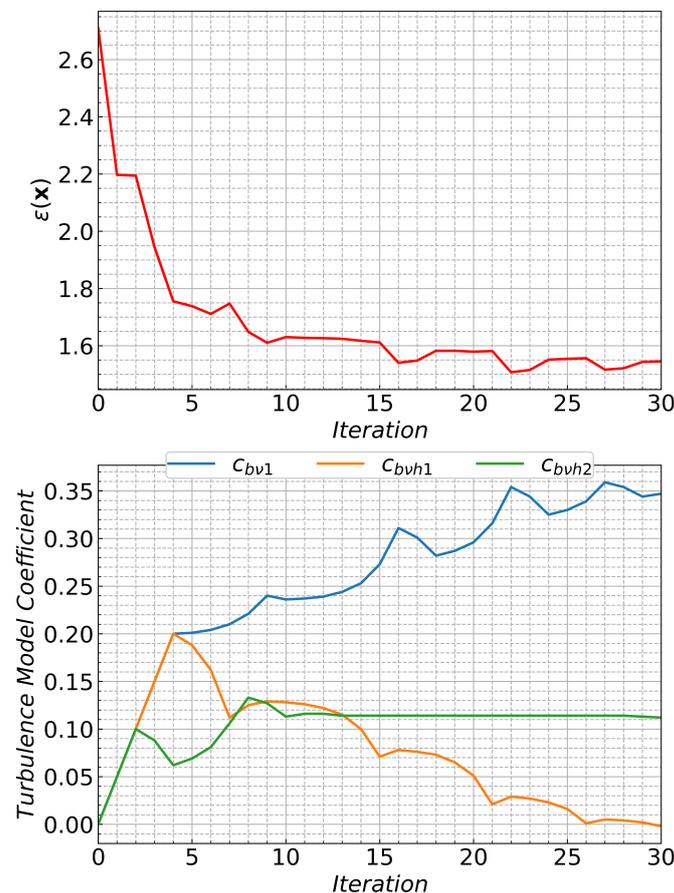
Figure 6. Sample optimization results. In the top part, the objective function $\mathcal{E}(x)$ (Equation (5)) versus optimization iterations is shown. In the lower part, the corresponding turbulence model coefficients are plotted.

6. Hybrid Neural Network

The ultimate goal of this study is to implement a machine learning framework that can predict the additional turbulence model coefficients based on a small number of inputs rather than rely on the optimization procedure described in Section 5. Moioli et al., showed that an optimized set of turbulence model coefficients for one configuration case is not

necessarily beneficial for a similar problem [20]. Further, experimental reference values for the needed or selected design points are not always available. Thus, the optimization routine is not applicable if the enhanced turbulence model should be deployed in large-scale production or applied for many different cases, e.g., in an early aircraft design phase with new configuration types.

The basic idea is to design a machine learning framework to predict selected additional turbulence model coefficients. This data model outputs the proper set of coefficients based on the geometrical properties of the configuration under investigation, flow, or flight parameters. The proposed hybrid neural network (HNN) is depicted in Figure 7. The neural network consists of a CNN segment, a fully connected layer with additional inputs, and an attached feed-forward neural network part.
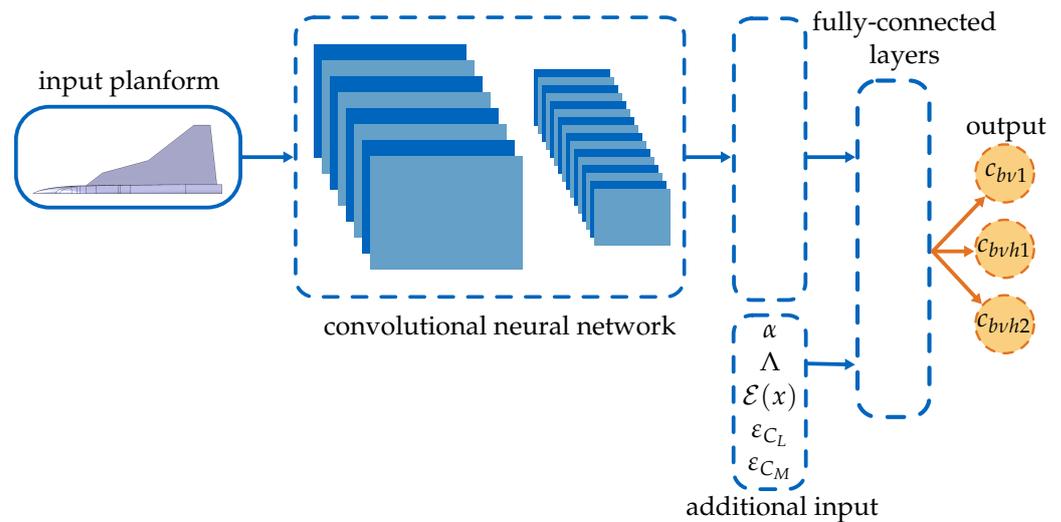
Figure 7. Schematic chart of the HNN.

A CNN is used for the geometry recognition and feature extraction to achieve maximum flexibility with respect to the input geometry. CNNs are known for their vast capabilities in image and pattern recognition, which enables the prediction framework to be independent of the input configuration. Rather than hard-coded input neurons for different geometric properties, a simple graphic of the wing-body plan form of the configuration is read in and propagated through several convolutional layers, including max-pooling and layer normalization. This architecture allows one network to be used for all thinkable cases since, e.g., a single delta wing configuration would have only one leading-edge sweep angle as a parameter, whereas in contrast, a triple delta wing configuration would have three distinct leading-edge sweep angles as input. Although high-aspect ratio wings are not part of the intended use cases, the implemented network could be fed with a plan form of the NASA Common Research Model (CRM). In the fully connected layer, the output of the CNN is combined with additional inputs. These inputs include the angle of attack α and the Mach number M_∞, and since the graphics of the input plan forms are not in scale, the aspect ratio Λ is added. Due to the relatively small training data set, each iteration of each case optimization serves as a data point. To differentiate between proper coefficients and unwanted sets of coefficients during training, the objective function $\mathcal{E}(x)$ as well as the errors between numerical and experimental aerodynamic coefficients ε_{C_L} and ε_{C_M} are added as inputs. The turbulence model coefficients are predicted in the final output layer after a series of hidden layers in a feed-forward neural network segment.

Hyperparameter Optimization and Training

The hyperparameter optimization is realized using the Optuna framework [21]. As a define-by-run optimization framework, Optuna has been mainly developed for the hyperparameter optimization of neural networks. The efficient implementation and the

versatile architecture, which enable an easy setup of the optimization runs, are critical elements of the software. The framework implements a Tree-structured Parzen Estimator (TPE) algorithm with an additional pruning mechanism. Pruning itself can be seen as an early-stopping method, where the algorithm detects automatically if the current trial shows promising results compared to a set of earlier trials or if the current trial should be canceled and another trial with a new set of hyperparameters should be started [21]. Table 2 lists the most important hyperparameters of the HNN.

Table 2. Overview of HNN hyperparameters.

Hyperparameter	
Initial learning rate	0.001
Batch size	4
Convolutional layers	3
Number of conv channels	8
Dimension fully connected layer	2367
Hidden layers	4

The available trainings dataset was obtained by conducting coefficient optimizations (Section 5) for different configurations of the introduced generic planforms in Section 2. For a total number of five double and five triple delta wings, the additional turbulence model coefficients have been obtained by optimization for the two design points $\alpha = 24°$ and $\alpha = 32°$. The final dataset included ≈ 800 datapoints and was split into 90% training and 10% validation during runtime.

Prior to the start of the training process, all data concerning the generic triple delta wing designated by F3 527552 STLong LV00 SL00 FL00 are excluded from the dataset and used for testing after finished training. The results for this configuration will be shown and discussed in Section 7.

7. Results

The results of the preconditioning performance and the corresponding CFD results are discussed in the following. The generic triple delta wing planform F3 527552 STLong LV00 SL00 FL00 has been excluded from the training and validation sets for the proposed HNN. It is, therefore, implemented as the final test case.

Table 3 lists the predicted turbulence model coefficient of the HNN for the triple delta wing. The optimized type refers to the original turbulence model coefficients resulting from the optimization procedure (Section 5) and the augmented type to the HNN predicted coefficients. Comparing the listed coefficients in Table 3, it can be seen that for the angle of attack, $\alpha = 24°$, all three additional turbulence model coefficients are predicted rather well. c_{bv1} matches nearly perfectly, where the coefficients c_{bvh1} and c_{bvh2} show minor deviations from the optimized values. For the angle of attack, $\alpha = 32°$ c_{bvh2} is predicted almost perfectly, where now c_{bv1} experiences a slight under-prediction when compared to the optimized coefficient. For this angle of attack, the coefficient c_{bvh1} is mispredicted and exceeds the optimized value by more than double the valuation. Despite various attempts at additional hyperparameter tuning, neural network training runs, and detailed dataset analysis, it was impossible to find a setting where some of the coefficients were not noticeable off the target value. The cause of these mispredictions has not been identified yet and will be subject to future work.

The integral aerodynamic coefficients for wind tunnel experiments and the CFD simulations with the standard SA model and the augmented enhanced SA model are listed in Table 4. Additionally, for the numerical results, the percentile deviation from the corresponding experimental coefficient is listed.

Table 3. Predictions of additional turbulence model coefficients.

	Type	c_{bv1}	c_{bvh1}	c_{bvh2}
$\alpha = 24°$	optimized	0.2	0.14	0.17
	augmented	0.21	0.11	0.14
$\alpha = 32°$	optimized	0.16	0.07	0.16
	augmented	0.135	0.175	0.15

For $\alpha = 24°$, the lift coefficient C_L is already resolved very well by the standard SA model, with a slight error of -1.6%. The augmented model underestimated the lift coefficient by -2.3%, which is still in excellent agreement. Due to the complex vortex flows, the pitching moment coefficient C_M is especially difficult to correctly resolve with standardized RANS models since it also relies on the spatial resolution of the surface pressure distribution. This difficulty can also be seen in Table 4, where the standard SA model overestimates the pitching moment coefficient by 15%. The augmented SA version cuts the pitching moment error nearly in half compared to the standard model, resulting in a lower deviation of 8.8%.

The results for the angle of attack $\alpha = 32°$ show that the augmented turbulence model underestimates the lift coefficient by -4.7% compared to a 0.7% overestimation by the original turbulence model. On the other hand, the pitching moment coefficient error is cut nearly in half by the augmented model. The original model results in a 28.5% deviation, whereas the augmented model reduces this error to 15.9%.

Table 4. Comparison of the aerodynamic coefficients of experimental and numerical data.

		C_L	$\Delta C_L [\%]$	C_M	$\Delta C_M [\%]$
	experimental	1.28	-	0.114	-
$\alpha = 24°$	standard SA	1.26	-1.6	0.131	15
	augmented SA	1.25	-2.3	0.124	8.8
	experimental	1.5	-	0.151	-
$\alpha = 32°$	standard SA	1.51	0.7	0.194	28.5
	augmented SA	1.43	-4.7	0.175	15.9

7.1. Pressure Distribution

The pressure distribution on the wing suction side for the triple delta wing F3 527552 STLong LV00 SL00 FL00 is depicted in Figure 8 for the angle of attack $\alpha = 24°$ and in Figure 9 for $\alpha = 32°$. The numerical result corresponding to the original SA model is on the left side of the figures. In the middle subfigure, the results of the augmented enhanced SA model are depicted in the right-hand subfigure numerical results of a high-fidelity delayed Detached Eddy Simulation (DDES) and are shown for reference.

Comparing the two RANS models (Figure 8a,b), some small changes in the suction peak distribution on the main wing can be seen. The enhanced turbulence model shows lower pressure coefficient values in the front section of the main wing, similar to the high-fidelity DDES results. Looking at Figure 8c as a reference, the standard turbulence model underestimates the pressure coefficient in the rear part of the main wing, whereas the enhanced turbulence model shows a little higher pressure distribution in this area. Further, the low-pressure area on the strake section caused by the formation of the inboard vortex (IBV) shows a similar downstream distribution for the enhanced model and the DDES, whereas the suction peak for the standard model is further extended downstream from the strake section. The results for $\alpha = 32°$ in Figure 9 show more differences for the different RANS turbulence model than for $\alpha = 24°$ in Figure 8. While the pressure distribution for the standard model in Figure 9a is very homogenous, the results for the enhanced turbulence model in Figure 9b display some irregular patterns, with several distinct suction peaks distributed over the whole wing surface. This behavior can also

be seen in the high-fidelity DDES result in Figure 9c. The pressure distribution over the strake section is similar for the enhanced model and the DDES results, where the enhanced turbulence model underestimates the pressure coefficient in the rear part of the strake section before the kink to the main wing section. The DDES result shows only a moderate suction peak in this area, whereas the enhanced turbulence model shows high negative C_P values. Comparing the main wing section between these two models, the enhanced turbulence model better represents the pressure distribution and the suction peak. While the suction peak is located slightly upstream of the main wing compared to the DDES result, strength, resolution, and distribution are quite similar between the RANS model and the high-fidelity simulation. The different pressure distributions show that the enhanced turbulence model results in a more detailed resolution than the original SA model. While the plots of $\alpha = 24°$ in Figure 8 show slight differences, the plots in Figure 9 for $\alpha = 32°$ show significant differences in pressure distribution over the wing surface. The improved results for the pitching moment coefficient introduced in Section 7 (Table 4) are rooted in the enhanced resolution of the adaptive turbulence model.
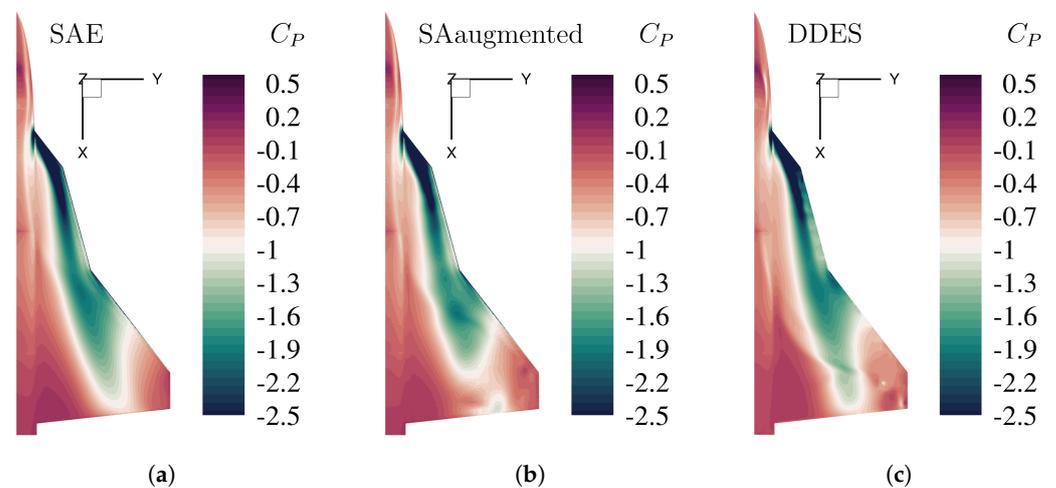
Figure 8. Surface pressure distribution by the means of pressure coefficient C_P at Mach number $M_\infty = 0.15$, Reynolds number $Re = 3 \cdot 10^6$, and angle of attack $\alpha = 24°$, for different numerical turbulence models. (**a**) Original SA model with Edwards-modification. (**b**) Enhanced SA model with augmented model coefficients (Table 3). (**c**) High-fidelty DDES reference simulation.

Figure 9. Surface pressure distribution by the means of pressure coefficient C_P at Mach number $M_\infty = 0.15$, Reynolds number $Re = 3 \cdot 10^6$, and angle of attack $\alpha = 32°$, for different numerical turbulence models. (**a**) Original SA model with Edwards-modification. (**b**) Enhanced SA model with augmented model coefficients (Table 3). (**c**) High-fidelty DDES reference simulation.

7.2. Total Pressure Loss

In this subsection, the vortical flow field is analyzed utilizing an isosurface of 2% total pressure loss $(p_t - p_{t,\infty})/p_{t,\infty}$ depicted in Figure 10 for the angle of attack $\alpha = 24°$ and for $\alpha = 32°$ in Figure 11. The isosurface is colored in the non-dimensional axial velocity profile u/U_∞, and stagnating or reversed flow is highlighted by a black isosurface representing areas of $u/U_\infty \leq 0$. As in Section 7.1, results for the numerical results based on the standard SA turbulence model are shown in the left-hand subfigures, and high-fidelity DDES reference results are shown in the right-hand subfigures. The results of the augmented enhanced turbulence model are depicted in the middle subfigures of Figures 10 and 11.

Comparing the RANS models in Figure 10a,b, it can be seen that the adaptive turbulence model shows some vortical flow structure, whereas the standard turbulence model results in a straight smooth isosurface for the total pressure loss. The original turbulence model shows a slightly wider cross-section area of the isosurface over the rear part of the main wing, meaning more total pressure is dissipated by the turbulence model in the flow field compared to the other two models. Focusing on the red spots representing maxima of the non-dimensional axial velocity, it can also be seen that the enhanced turbulence model transports these maxima further downstream, sustaining more energy in the flow field. Although the DDES result in Figure 10c contains a more detailed resolution, the enhanced turbulence model shows an almost similar distribution of the total pressure loss.
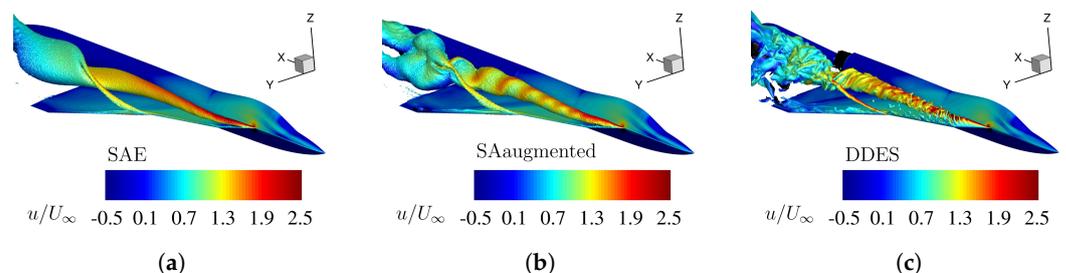
Figure 10. Flow field visualization by an isosurface of 2% total pressure loss $(p_t - p_{t,\infty})/p_{t,\infty}$ at Mach number $M_\infty = 0.15$, Reynolds number $Re = 3 \cdot 10^6$, and angle of attack $\alpha = 24°$, for different numerical turbulence models. The isosurface is colorized by the non-dimensional axial velocity u/U_∞. (**a**) Original SA model with Edwards-modification. (**b**) Enhanced SA model with augmented model coefficients (Table 3). (**c**) High-fidelty DDES reference simulation.

At $\alpha = 32°$ the results in Figure 11 highlight the differences between original and enhanced turbulence models. Neglecting the resolution differences, Figure 11b shows nearly the same total pressure loss distribution as the high-fidelity DDES result in Figure 11c. The vortical flow structure and the distribution of the non-dimensional axial velocity are more or less identical, whereas the maxima of non-dimensional axial velocity depicted in red are dissipated approximately at the exact location downstream of the kink between the strake and main wing sections. Vortex breakdown and the irregular flow field are visible over the main wing section for the enhanced turbulence model. The original turbulence model shows a smooth, straight isosurface with no vortical flow structures present. Additionally, it can be seen that the maxima of the non-dimensional axial velocity is dissipated further upstream compared to the other two numerical model.

The results of total pressure loss highlight the different capabilities of vortical flow representation between the original turbulence model and the enhanced turbulence model with additional source terms.
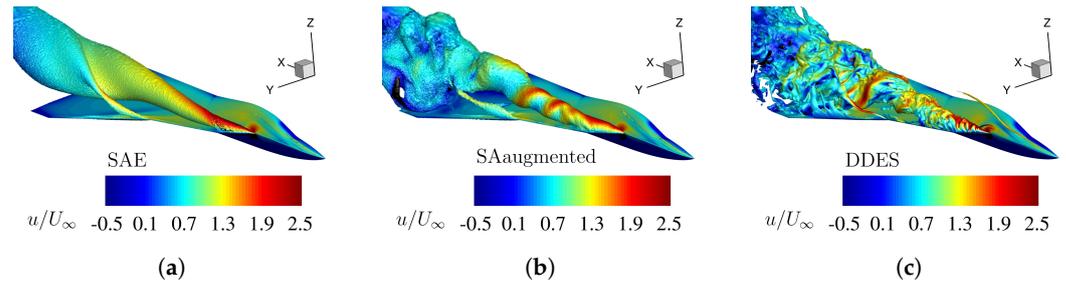
Figure 11. Flow field visualization by an isosurface of 2% total pressure loss $(p_t - p_{t,\infty})/p_{t,\infty}$ at Mach number $M_\infty = 0.15$, Reynolds number $Re = 3 \cdot 10^6$, and angle of attack $\alpha = 32°$, for different numerical turbulence models. The isosurface is colorized by the non-dimensional axial velocity u/U_∞. (**a**) Original SA model with Edwards-modification. (**b**) Enhanced SA model with augmented model coefficients (Table 3). (**c**) High-fidelty DDES reference simulation.

7.3. Normalized Q-Criteria

Another possibility to visualize the rotational flow field is to plot the isosurface of the Q-criterion. A vortex can be defined as a connected fluid region with a positive second invariant of the velocity gradient [22,23]. Following Equation (5):

$$Q = \frac{1}{2}\left(u_{i,i}^2 - u_{i,j}u_{j,i}\right) = -\frac{1}{2}u_{i,j}u_{j,i} = \frac{1}{2}\left(||\mathbf{\Omega}||^2 - ||\mathbf{S}||^2\right) \tag{5}$$

it defines the regions where the vorticity magnitude exceeds the strain-rate magnitude. In Figures 12 and 13, the isosurface of the normalized Q-criterion $Q^* = (Q \cdot l_\mu^2)/U_\infty = 50$ colorized by the means of total pressure ratio $p_t/p_{t,\infty}$ is shown for the angles of attack $\alpha = 24°$ and $\alpha = 32°$, respectively, where l_μ is defined as the mean aerodynamic chord. Additionally, regions of stagnating or reversed flow are marked by a black isosurface representing $u/U_\infty \leq 0$.

Comparison of the RANS turbulence models in Figure 12a,b shows that the normalized Q-criterion for enhanced turbulence model resolves more vortical structures similar to the high-fidelity DDES results in Figure 12c than the original model. The outboard region of the main wing section especially experiences no vortex flow with the standard turbulence model. Another sign of the improved turbulent diffusion of the enhanced turbulence model is the distribution of the inboard nose vortex. While the nose vortex of the original model is dissolved in the strake section, the nose vortex for the enhanced model extends further downstream and connects with the IBV over the main wing, which can also be seen in the high-fidelity data.

At $\alpha = 32°$ in Figure 13, vortex breakdown is already present, and the standard SA turbulence model fails to resolve any vortical structure exceeding the break-up of the IBV over the strake section. Comparing the three subfigures, it is noticeable that the enhanced turbulence model in Figure 13b is far more similar to the high-fidelity DDES result in Figure 13c than to the result of the standard turbulence model. Although vortex breakdown is present, the additional source terms (especially c_{bvh2}) enable the turbulence model to resolve the vortex structures in more detail. At this angle of attack, the leading-edge vortex's strong formation can be seen through a spiral-type vortical structure. High energetic flow, which can be identified by $p_t/p_{t,\infty} \geq 1$, is transported further downstream by the enhanced turbulence model. Downstream of vortex breakdown, the RANS model still shows more dissipation, and the vortical structures dissolve totally over the main wing. In contrast, the DDES suggests that the structures exceed the trailing edge.
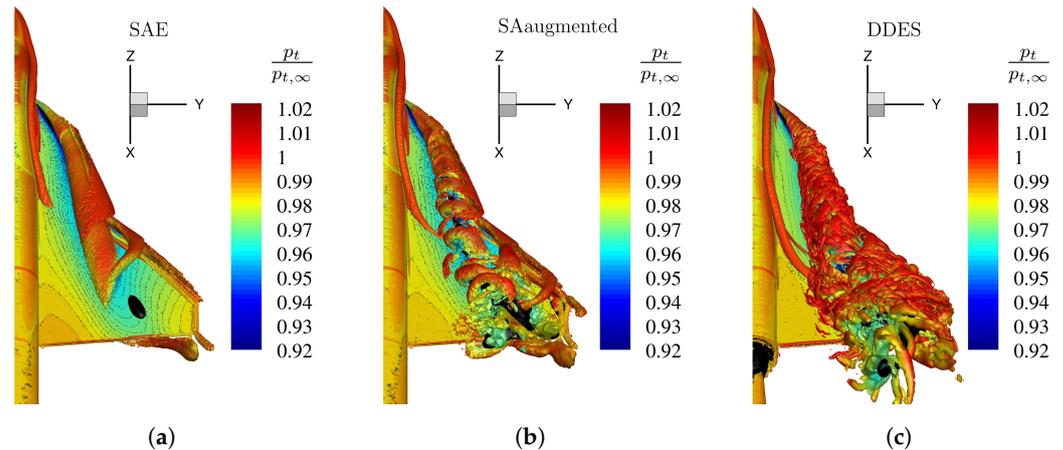
Figure 12. Visualization of vortical structures by an isosurface of the normalized Q-criterion $Q^* = (Q \cdot l_\mu^2)/U_\infty$ at Mach number $M_\infty = 0.15$, Reynolds number $Re = 3 \cdot 10^6$, and angle of attack $\alpha = 24°$, for different numerical turbulence models. The isosurface is colorized by the total pressure ratio $p_t/p_{t,\infty}$. (**a**) Original SA model with Edwards-modification. (**b**) Enhanced SA model with augmented model coefficients (Table 3). (**c**) High-fidelty DDES reference simulation.
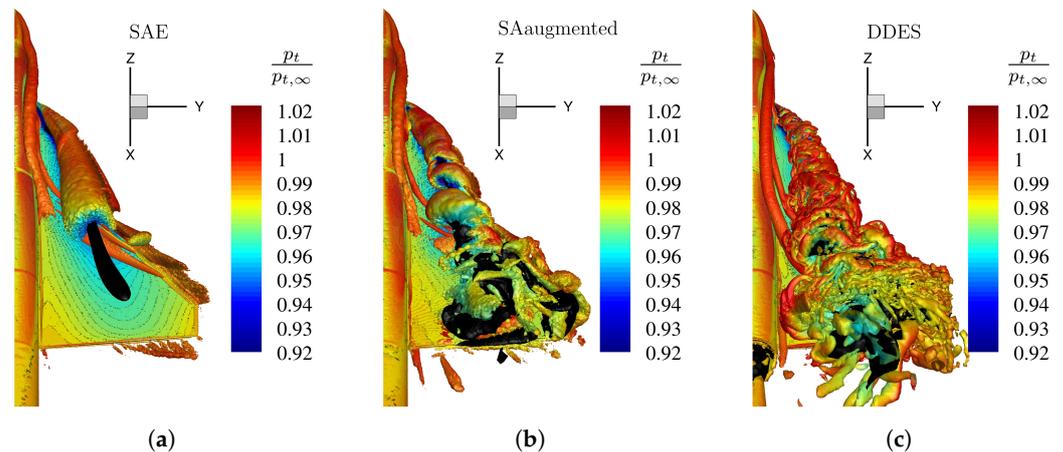
Figure 13. Visualization of vortical structures by an isosurface of the normalized Q-criterion $Q^* = (Q \cdot l_\mu^2)/U_\infty$ at Mach number $M_\infty = 0.15$, Reynolds number $Re = 3 \cdot 10^6$, and angle of attack $\alpha = 32°$, for different numerical turbulence models. The isosurface is colorized by the total pressure ratio $p_t/p_{t,\infty}$. (**a**) Original SA model with Edwards-modification. (**b**) Enhanced SA model with augmented model coefficients (Table 3). (**c**) High-fidelty DDES reference simulation.

7.4. Vortex Bursting

The accurate prediction of vortex breakdown and vortex breakdown positions is directly linked to the adverse pressure gradient handling of the turbulence model. Leading-edge vortices experience breakdown at high angles of attack due to the stagnation of the axial core flow caused by the adverse pressure gradient along the vortex core axis [24]. In the following, the comparison of reversed flow profiles for the three different numerical methods is discussed. In Figure 14, the results for the angle of attack $\alpha = 24°$ are presented, and in Figure 15, the results for $\alpha = 32°$, respectively. The reversed flow characteristic is analyzed using an isosurface representing regions, where the non-dimensional axial velocity $u/U\infty \leq -0.1$. The surface distribution for the total pressure ratio $p_t/p_{t,\infty}$ is shown.

Compared to the isosurface of the high-fidelity numerical result in Figure 14c, it is obvious that the standard SA turbulence model is unable to resolve reversed flow (Figure 14a). On the other hand, the enhanced turbulence model shows similar reverse flow behavior like the DDES data. Especially the on-set position and downstream extent match the high-fidelity data nearly perfectly.

(a)   **(b)**   **(c)**
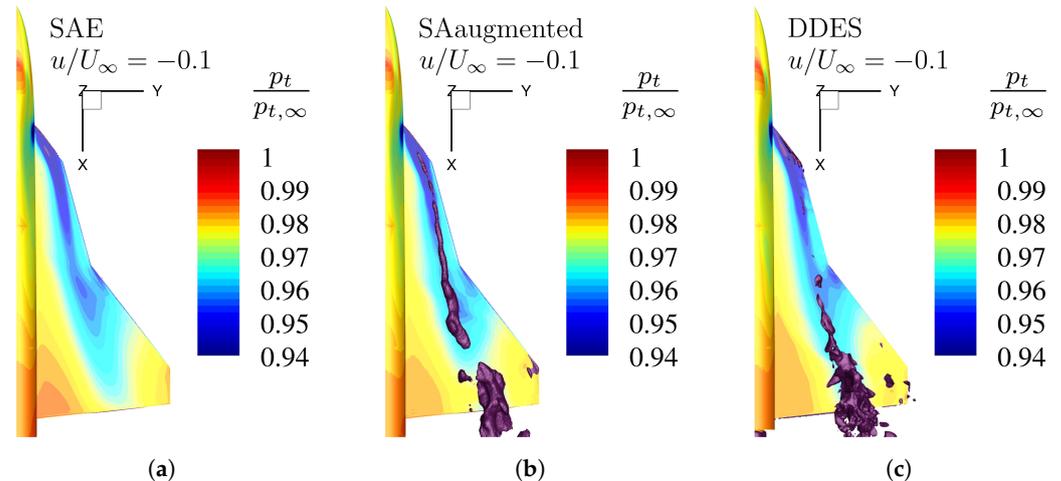
Figure 14. Reverse flow regions by an isosurface of the non-dimensional axial velocity $u/U_\infty \leq -0.1$ at Mach number $M_\infty = 0.15$, Reynolds number $Re = 3 \cdot 10^6$, and angle of attack $\alpha = 24°$, for different numerical turbulence models. Additionally, the surface total pressure ratio distribution $p_t/p_{t,\infty}$ is shown. (**a**) Original SA model with Edwards-modification. (**b**) Enhanced SA model with augmented model coefficients (Table 3). (**c**) High-fidelty DDES reference simulation.

The same analyses can be carried out for the angle of attack $\alpha = 32°$. Figure 15 shows that the original turbulence model resolves no reversed flow, while the enhanced turbulence matches the flow characteristics of the high-fidelity results. Although the downstream variation of the isosurfaces cross-section varies differently between these two numerical models, the extent over the whole wing area is present for both models. To better understand the capabilities of the enhanced SA turbulence model, the isosurface of the non-dimensional axial velocity $u/U\infty \leq -0.6$ is shown in Figure 16 for the angle of attack $\alpha = 32°$. Since in Figure 15 it is already presented that the original SA model is not capable of resolving this flow characteristic, only the results for the enhanced model and the DDES simulation are presented. $u/U\infty \leq -0.6$ represents regions with strong reversed flow. Comparing the two different numerical approaches, it can be seen that at this magnitude, the RANS model does not represent similar reverse flow structures like the DDES model. This means that the enhanced model shows better resolution capabilities when compared to the original turbulence model but still embodies a higher numerical dissipation than the high-fidelity simulation approach.

(a)   **(b)**   **(c)**
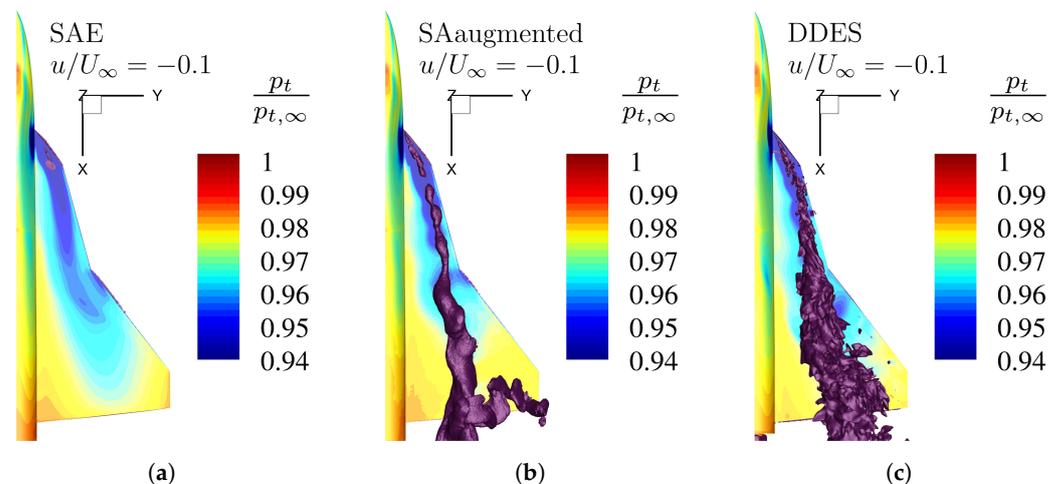
Figure 15. Reverse flow regions by an isosurface of the non-dimensional axial velocity $u/U_\infty \leq -0.1$ at Mach number $M_\infty = 0.15$, Reynolds number $Re = 3 \cdot 10^6$, and angle of attack $\alpha = 32°$, for different numerical turbulence models. Additionally, the surface total pressure ratio distribution $p_t/p_{t,\infty}$ is shown. (**a**) Original SA model with Edwards-modification. (**b**) Enhanced SA model with augmented model coefficients (Table 3). (**c**) High-fidelty DDES reference simulation.
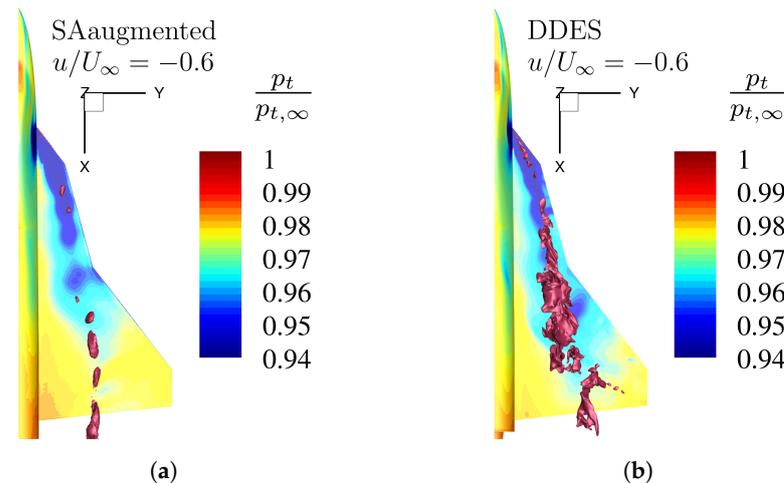
Figure 16. Detailed reverse flow regions by an isosurface of the non-dimensional axial velocity $u/U_\infty \leq -0.6$ at Mach number $M_\infty = 0.15$, Reynolds number $Re = 3 \cdot 10^6$, and angle of attack $\alpha = 32°$, for different numerical turbulence models. Additionally, the surface total pressure ratio distribution $p_t/p_{t,\infty}$ is shown. (**a**) Enhanced SA model with augmented model coefficients (Table 3). (**b**) High-fidelty DDES reference simulation.

In summary, the enhanced turbulence model shows the improved capabilities of reversed flow prediction due to the additional source terms. The proper resolution of this flow feature is important to define the vortex breakdown position and thus properly predict pressure distributions and, as a result, the pitching moment coefficient.

8. Conclusions and Outlook

This study presented the preconditioning capabilities of an HNN framework concerning an adaptive turbulence model based on the standard SA turbulence model. The enhanced turbulence model includes additional source terms linked to a so-called vortex identifier quantity to affect vortex-dominated flow regions only. Model coefficients like those in the original SA model further control the additional source terms. An optimal set of these coefficients can be obtained through an automated optimization process, which needs corresponding computational effort due to the high number of necessary CFD simulations. This work describes the possibility of preconditioning this turbulence model via a machine learning framework rather than relying on the costly optimization procedure. The neural network itself is independent of the underlying input configuration. While the adaptive turbulence model was designed with special emphasis on leading-edge vortex flow systems of medium to low aspect ratio delta wings, the neural network can be fed with any configuration.

The results of the network tests show that the proposed architecture can predict a proper turbulence model coefficient set quite accurately. Most predicted turbulence coefficients are close to their true values, defined by an out-of-the-loop optimization run. The test run also showed that due to the currently available small dataset, the neural network sometimes off-predicts one of the three tested turbulence model coefficients. The reason for this selective misprediction has yet to be found and will be included in future works.

The assessment of improvement is presented employing a comparison of CFD simulation results based on the original SA model, the enhanced SA model, and a high-fidelity DDES simulation. The comparison shows that the enhanced turbulence model with augmented model coefficients improves the resolution of the flow field. Vortical structures, pressure distribution, and reversed flow characteristics are resolved in more detail than for the original turbulence model. The results for the aerodynamic coefficients show that especially the pitching moment coefficient is computed with higher precision due to the improved accuracy in the surface pressure distribution.

In future works, the accuracy of prediction and preconditioning shall be improved by increasing the available training dataset. The dataset and preconditioning framework shall also be tested for different Mach numbers and configurations outside of this work using a generic multiple-swept delta wing platform.

Author Contributions: Conceptualization, M.Z. and C.B.; Methodology, M.Z.; Software, M.Z.; Validation, M.Z.; Formal analysis, M.Z.; Investigation, M.Z.; Resources, M.Z.; Data curation, M.Z.; writing—original draft, M.Z.; writing—review and editing, M.Z. and C.B.; Visualization, M.Z.; Supervision, C.B.; Project administration, C.B.; Funding acquisition, C.B. All authors have read and agreed to the published version of the manuscript.

Data Availability Statement: The data supporting the conclusions of this article will be made available by the authors on request.

Conflicts of Interest: The authors declare no conflict of interest.

References

1. Shur, M.L.; Strelets, M.K.; Travin, A.K.; Spalart, P.R. Turbulence Modeling in Rotating and Curved Channels: Assessing the Spalart-Shur Correction. *AIAA J.* **2000**, *38*, 784–792. [CrossRef]
2. Smirnov, P.E.; Menter, F.R. Sensitization of the SST Turbulence Model to Rotation and Curvature by Applying the Spalart–Shur Correction Term. *J. Turbomach.* **2009**, *131*, 041010. [CrossRef]
3. Menter, F.R. Two-equation eddy-viscosity turbulence models for engineering applications. *AIAA J.* **1994**, *32*, 1598–1605. [CrossRef]
4. Arolla, S.K.; Durbin, P.A. Modeling rotation and curvature effects within scalar eddy viscosity model framework. *Int. J. Heat Fluid Flow* **2013**, *39*, 78–89. [CrossRef]
5. Moioli, M.; Breitsamter, C.; Sørensen, K.A. Parametric data-based turbulence modelling for vortex dominated flows. *Int. J. Comput. Fluid Dyn.* **2019**, *33*, 149–170. [CrossRef]
6. Spalart, P.; Allmaras, S. A one-equation turbulence model for aerodynamic flows. In Proceedings of the 30th Aerospace Sciences Meeting and Exhibit, Reno, NV, USA, 6–9 January 1992. [CrossRef]
7. Duraisamy, K.; Iaccarino, G.; Xiao, H. Turbulence Modeling in the Age of Data. *Annu. Rev. Fluid Mech.* **2018**, *51*, 357–377. [CrossRef]
8. Bengio, Y. Learning Deep Architectures for AI. *Found. Trends Mach. Learn.* **2009**, *2*, 1–127. [CrossRef]
9. Sabater, C.; Stürmer, P.; Bekemeyer, P. Fast Predictions of Aircraft Aerodynamics Using Deep-Learning Techniques. *AIAA J.* **2022**, *60*, 5249–5261. [CrossRef]
10. Zahn, R.; Winter, M.; Zieher, M.; Breitsamter, C. Application of a long short-term memory neural network for modeling transonic buffet aerodynamics. *Aerosp. Sci. Technol.* **2021**, *113*, 106652. [CrossRef]
11. Hitzel, S.M.; Winkler, A.; Hövelmann, A. Vortex Flow Aerodynamic Challenges in the Design Space for Future Fighter Aircraft. In *Notes on Numerical Fluid Mechanics and Multidisciplinary Design*; Springer: Berlin/Heidelberg, Germany, 2019; pp. 297–306. [CrossRef]
12. Pfnür, S.; Pflüger, J.; Breitsamter, C. Analysis of Vortex Flow Phenomena on Generic Delta Wing Planforms at Subsonic Speeds. In *Notes on Numerical Fluid Mechanics and Multidisciplinary Design*; Springer: Berlin/Heidelberg, Germany, 2019; pp. 328–337. [CrossRef]
13. Hövelmann, A.; Winkler, A.; Hitzel, S.M.; Richter, K.; Werner, M. Analysis of Vortex Flow Phenomena on Generic Delta Wing Planforms at Transonic Speeds. In *Notes on Numerical Fluid Mechanics and Multidisciplinary Design*; Springer: Berlin/Heidelberg, Germany, 2019; pp. 307–316. [CrossRef]
14. Guilmineau, E.; Visonneau, M. Evaluation of turbulence modelling for subsonic vortex interaction on multi delta wing configuration. In Proceedings of the 56th 3AF International Conference on Applied Aerodynamics, Toulouse, France, 28–30 March 2022.
15. Visonneau, M.; Guilmineau, E.; Wackers, J. Computational Analysis of Subsonic Vortex Interaction on Multi Swept Delta Wing Configurations. In Proceedings of the AIAA SCITECH 2022 Forum, San Diego, CA, USA, 3–7 January 2022. [CrossRef]
16. Schwamborn, D.; Gerhold, T.; Heinrich, R. The DLR TAU-Code: Recent Applications in Research and Industry. In ECCOMAS CFD 2006: Proceedings of the European Conference on Computational Fluid Dynamics, Egmond aan Zee, The Netherlands, 5–8 September 2006; pp. 1–25.
17. Truesdell, C. The physical components of vectors and tensors. *J. Appl. Math. Mech.* **1953**, *33*, 345–356. [CrossRef]
18. Jeong, J.; Hussain, F. On the identification of a vortex. *J. Fluid Mech.* **1995**, *285*, 69–94. [CrossRef]
19. Nelson, R.C.; Visser, K.D. Breaking Down the Delta Wing Vortex: The Role of Vorticity in the Breakdown Process. In Proceedings of the AGARD Symposium on Vortex Flow Aerodynamics, Scheveningen, The Netherlands, 1–4 October 1990; Ph.D. Thesis Final Report.1991.

20. Moioli, M.; Breitsamter, C.; Sørensen, K.A. Turbulence Modeling for Leading-Edge Vortices: An Enhancement based on Experimental Data. In Proceedings of the AIAA Scitech 2020 Forum, Orlando, FL, USA, 6–10 January 2020. [CrossRef]

21. Akiba, T.; Sano, S.; Yanase, T.; Ohta, T.; Koyama, M. Optuna: A Next-generation Hyperparameter Optimization Framework. In Proceedings of the 25th ACM SIGKDD International Conference on Knowledge Discovery and Data Mining, Anchorage, AK, USA, 4–8 August 2019.

22. Lee, M.J.; Hunt, J.C.R. The structure of sheared turbulence near a plane boundary. In *Studying Turbulence Using Numerical Simulation Databases—II, Proceedings of the 1988 Summer Program, Stanford, CA, USA, 27 June–22 July 1988*; Ames Research Center, National Aeronautics and Space Administration (NASA): Mountain View, CA, USA; Center for Turbulence Research (CTR), Stanford University: Stanford, CA, USA. Available online: https://ntrs.nasa.gov/citations/19890015186 (accessed on 24 January 2024)

23. Kolář, V. Vortex identification: New requirements and limitations. *Int. J. Heat Fluid Flow* **2007**, *28*, 638–652. [CrossRef]

24. Mitchell, A.; Molton, P.; Barberis, D.; Delery, J. Characterization of vortex breakdown by flow field and surface measurements. In Proceedings of the 38th Aerospace Sciences Meeting and Exhibit, Reno, NV, USA, 10–13 January 2000. [CrossRef]